

Title:

Tribological behavior of self-lubricating carbon nanoparticle reinforced metal matrix composites

Authors:

Leander Reinert, Itzhak Green, Steffen Gimmler, Björn Lechthaler, Frank Mücklich, Sebastian Suárez

This is the accepted manuscript of an article published in *Wear* (Volume 408-409, 2018, Pages 72-85, DOI: 10.1016/j.wear.2018.05.003).

The version of record is available online at: <https://doi.org/10.1016/j.wear.2018.05.003>

This manuscript is distributed under the terms and conditions of the Creative Commons License CC BY-NC-ND 4.0 (<https://creativecommons.org/licenses/by-nc-nd/4.0/>).



Tribological behavior of self-lubricating carbon nanoparticle reinforced metal matrix composites

L. Reinert^{1,*}, I. Green², S. Gimmmler¹, B. Lechthaler¹, F. Mücklich¹, and S. Suárez¹

¹Department of Materials Science, Saarland University, Campus D3.3, D-66123, Saarbrücken, Germany

²George W. Woodruff School of Mechanical Engineering, Georgia Institute of Technology, Atlanta, USA

Abstract

The present study focuses on investigating the dominant friction and wear mechanisms in case of dry sliding of carbon nanoparticle reinforced nickel matrix composites under elastic and elasto-plastic contact conditions. For this purpose, multi-wall carbon nanotubes (CNT), onion-like carbon (OLC) and nanodiamonds (nD) were chosen to represent a large variety of carbon nanoparticles as they can be systematically distinguished regarding their carbon hybridization state (sp^2 vs. sp^3) as well as their morphology and size (“0D” vs. “1D”). Contact simulations based on the Greenwood-Williamson model are conducted in order to calculate the required contact loads. Friction and wear analysis is supported by complementary characterization techniques, including scanning electron microscopy, transmission electron microscopy, energy dispersive spectroscopy, Raman spectroscopy, light microscopy as well as laser scanning microscopy. It is found, that only CNT provide efficient lubrication as reinforcement phase in composites, presenting different lubrication mechanisms for the tested contact conditions. The high aspect ratio of CNT is found to be essential for the lubrication mechanisms, allowing the particles to be dragged into the direct tribological contact. The lubrication effect increases with increasing volume content of CNT, reaching a maximum steady state frictional reduction of 50% compared to the unreinforced nickel reference.

Keywords

Carbon nanoparticles; Solid lubrication; Carbon nanotubes; Onion-like carbon; Nanodiamonds; Metal matrix composites

1 Introduction

Nowadays, the increasing demand for lower energy consumption in nearly every technical application sets the need for the tribological optimization of various technical components, like for example automotive parts such as cylinder liners, piston rings or bearings in passenger cars [1]. One way of approaching these problems is to reduce friction and wear by lubricating these systems, in most cases with a suitable liquid lubricant. However, due to their potential impact on the environment and low evaporation point, there is a trend to replace liquid with solid lubricants in certain mechanical systems [2,3]. Also, problems often arise when a constant oil supply cannot be achieved, a low oil pressure appears or oil leakage occurs which can lead to catastrophic failure of the

* Corresponding author. Tel/Fax: +49 (681) 302 70544/70502. Permanent address: Campus D3.3, Saarland University, Saarbrücken D-66123, Germany. E-mail address: l.reinert@mx.uni-saarland.de (L. Reinert)

lubricated system. Thus, new approaches to create self-lubricating materials, which are insensitive about their atmospheric surrounding and external influences, have to be developed in order to fit the elevated requirements. The possibility to tailor the physical and tribological properties of composite materials by variation of simple process parameters, the matrix or the reinforcement phase was extensively studied over the last decades. Beside of other reinforcement materials such as ceramics, MoS₂ or graphite, carbon nanomaterials are very promising reinforcement candidates in composites to increase strength [4–6], hardness [7–9], electrical and thermal conductivity [8,10,11] thermomechanical stability [12] and reduce friction and wear [13–17]. This is mainly due to their outstanding properties and low density compared to other reinforcement materials [18–20]. For our work, we focus on three types of carbon nanoparticles (CNPs), namely multi-wall carbon nanotubes (CNT) [21] nanodiamonds (ND) [20] and onion-like carbons (OLC) [22]. CNTs consist of helical hollow cylinders of graphitic carbon (sp²-hybridized) having multiple shells and a high aspect ratio (“one-dimensional”) [21]. The spherical diamond nanoparticles, named NDs, show a lattice spacing of 0.21 nm and feature a primary particle diameter of around 5 nm (“zero dimensional”) [20]. NDs can be transformed to OLC by thermal annealing in inert atmosphere or vacuum. OLCs, which are also known as carbon onions, are multi-shell, graphitic, fullerene nanoparticles (“zero dimensional”) with a typical spacing of 0.34–0.36 nm between the outer shells [22,23]. We chose these three particular CNPs as they show either a different carbon hybridization state or a different particle geometry/size, therefore representing a variety of carbon nanoparticles and allowing for a systematic investigation of the effect of those differences on the tribological properties of the composite material.

In case of CNTs, several works confirm the reduction in friction and/or wear when used as reinforcement phase in a metal matrix composite [16,24–27]. However, the tribo-mechanisms of the CNTs within these composites are still not fully understood. The effects might result from the influence of the CNTs on the microstructure of the composite. The particles could hinder the dislocation movement and therefore reduce plastic deformation of the surfaces. A higher strength, induced by a grain refinement effect (pinning effect) is also found to be a reason for a reduction in friction and wear. Typically, these effects are more pronounced for nanosized materials like for example CNT [28]. Furthermore, CNTs provide the ability to efficiently separate the sliding surfaces, slide or possibly act as roller bearings [29]. In this context, Dickrell et al. showed a frictional anisotropy effect of CNT coatings. Other studies have shown that the CNTs form a carbonaceous layer on the surface, which shows tribomechanisms similar to those of graphite [30,31]. Simulations at higher temperatures have shown, that there might be a pressure induced transformation of CNTs towards graphite when a pressure of about 1,5 – 2,5 GPa is applied [32]. However research works regarding this topic were conducted under different conditions and using different matrix materials, such as Cu, Al, Ni or the CNTs were applied as coating, for example on a SiO₂ substrate [5,24,27,33]. Thus, these findings leave it rather unclear how the lubrication mechanism in a composite type material reinforced with CNTs is working.

When it comes to NDs used as reinforcement phase in metal matrix composites, most of the research refers to a wear reducing effect instead of a frictional reduction [13,34–36]. A wear reduction can be traced back to an increased hardness of the composite by grain refinement. Furthermore, hindering of dislocation movement and also the hard particles themselves may contribute in a wear reduction of the composites [13,35]. However, NDs can also increase wear. An increased wear was ascribed to the breaking out of NDs from the matrix and consequently acting as abrasive third body within the tribological contact. On the other hand, NDs that are embedded in the matrix material could act as spacer between the two sliding surfaces and therefore prevent direct contact of the asperities [36]. The potential to act as roller bearing on top of a surface and thus to reduce

friction is controversially discussed in literature [13,34].

Considering OLCs, there is yet no available literature, which investigates their effect as reinforcement phase in a metallic composite material on the tribological properties. However, there is research claiming for very beneficial tribological properties of OLCs. Because of their polyhedral form and also their high mechanical strength, it is reasonable to assume that they might act as a roller bearings in a tribological contact [18]. Furthermore, as the curvature of OLCs is smaller compared to CNTs, it is supposed that they show less intermolecular interactions to other materials and thus being able to freely move on top of a surface [37,38]. Research in this field has been conducted by Hirata et al. [39], showing that on a silicon wafer, a very low friction coefficient lower than 0.05 can be achieved and also wear can be significantly reduced by 3 to 6 orders of magnitude compared to using graphite as lubricant. Also, in contrast to a lubrication using graphite, the lubrication effect by OLCs is not affected using vacuum conditions. However, there is a change in the effect as a function of the surface roughness, as the particles can be trapped within the asperities and therefore no longer provide a lubricating effect as they are not in direct contact in between the surfaces anymore [39]. Furthermore, simulations show a dependence of the lubrication effect of the OLCs from the applied contact pressure. If the pressure exceeds a value of 5 GPa (in case of two contacting DLC coated surfaces, that are lubricated by OLC), the lubrication effect significantly decreases [40].

To sum up, the variation in testing parameters, materials and conditions in literature make it rather difficult to correlate the measured effects to the underlying friction and/or wear mechanism of carbon nanoparticles. In the present study, a tribological comparison between the described three different CNPs as reinforcement phase in a nickel matrix composite is provided for elastic and elasto-plastic contact conditions under low (4%) and medium (45%) relative humidity. This is to learn about the acting lubrication mechanisms of the individual particles in a composite material, which can only be achieved in case of investigating systematically distinguishable CNPs as reinforcement phase in the same matrix material and under the same conditions. To the best of our knowledge, this is the first systematic comparison of the tribological properties of CNTs, OLCs, or NDs in a metal matrix.

A dispersion analysis of these particular CNPs in the composite as well as a model to control and predict the final microstructure after sintering was published by our work group before [41,42]. Based on these works, it is possible to produce composite materials reinforced by these CNPs, which feature the same final microstructure and hardness. Thus, the influence of the microstructure and hardness on the tribological properties could be neglected. Nickel appears to be a suitable candidate as matrix material for a comparative study, since it only forms metastable carbides under very specific conditions, as shown in a previous study reported by Suarez et al. [43].

In order to test the composites under varying mechanical contact situations (fully elastic or elasto-plastic), contact mechanics simulations need to be performed to calculate the corresponding necessary normal loads. One of the earliest models of elastic asperity contact is that of Greenwood and Williamson (G-W) [44]. This model uses the solution of the contact of an elastic hemisphere and a rigid flat plane, otherwise known as the Hertz contact solution, to stochastically model an entire contacting surface of asperities with a postulated Gaussian height distribution. The G-W model also assumes that the asperities do not interfere with adjacent asperities and that the bulk material below the asperities does not deform. Supplementing the G-W model, many elasto-plastic asperity models have been devised [45–48]. The G-W model is a statistical method, and hinges upon obtaining statistical parameters like the radius of curvature (R), the areal asperity density (η) and the standard deviation of the surface heights (σ). A way of finding these parameters is given by McCool, using the spectral moments in

order to calculate the aforementioned parameters [49]. In case of fully elastic contact conditions, the G-W model provides sufficiently accurate results for most of the engineering tasks and has gained wide acceptance. However, considering elasto-plastic contact conditions, the G-W model is not sufficient and it has to be extended. The contact conditions can be assessed by calculating the plasticity index ψ [44,48]. For cases where the plasticity index indicates elasto-plastic contact conditions, some early contact models have extended the venerable Greenwood-Williamson (G-W) model; these include, for example, the Kogut-Etsion (K-E) model [45], the Chang-Etsion-Bogy (CEB) model [46], or the Zhao-Maietta-Chang (ZMC) model [47]. A more recent model (that does not depend on limiting assumptions, e.g., material hardness) is developed by Jackson and Green (J-G model), producing predictions for contact area, contact force and surface separation [48,50]. Thus, in the present work, the J-G model is used in order to simulate the contact conditions in the given tribological system. The experimental work is done based on these simulations and various characterization methods are used with respect to the simulated contact regime.

In this regard, laser-scanning microscopy is used to generate the surface data on which the contact simulation is based upon. Furthermore, as a function of the given contact situation, the structural integrity of the particles is analyzed by Raman spectroscopy. Additionally, the obtained microstructure, and the resulting mechanical reinforcement effect are analyzed by scanning electron microscopy (SEM) and electron backscatter diffraction (EBSD). Finally, the generated wear tracks are analyzed by SEM and energy dispersive X-ray spectroscopy (EDS) in order to discuss the wear mechanisms as a function of the contact situation.

2 Materials and methods

2.1 Materials and manufacturing

Nickel matrix composites reinforced with CNT (Baytubes C150P from Bayer, purity > 95%, individual particle diameter of 5–20 nm, length of 2-10 μm), ND (NaBond Technologies Co., purity > 98%, individual particle diameter 4–8 nm), and nanodiamond-derived OLCs were produced by hot uniaxial pressing. To synthesize the OLCs, ND powder was annealed in graphite crucibles (30 mm in diameter and 20 mm in height) in a vacuum furnace with tungsten heaters (model: 1100-3580-W1, Thermal Technology Inc.) using a heating and cooling rate of 15 $^{\circ}\text{C}/\text{min}$. The transformation temperature was 1750 $^{\circ}\text{C}$ with a holding time of 3 h. The chamber pressure was between 10 mPa and 100 mPa.

The particles were blended with the nickel powder (Alfa Aesar, 325 mesh) using a colloidal mixing method, using ethylene glycol as solvent [41,43]. For the particle dispersion, a shear mixer (Ultra-Turrax T-25 by IKA) and subsequently an ultrasonic bath (Sonorex Super RK 514 BH by Bandelin, 860 W, 35 kHz) were used for 5 and 20 min, respectively. Afterwards, Ni is added and blended with the dispersed particles (particle fraction: 5, 10 and 20 vol.-% for each type) in the shear mixer for another 5 min.

As shown in reference [42], the CNP concentration strongly affects the composites' microstructure if near-full densification (> 98%) is achieved. With the aim of obtaining a simplified system, the sintering parameters were chosen so as to avoid differences in the microstructure of the matrix, irrespective of the type and amount of CNP [42]. Nonetheless, the parameters are sufficient to achieve a good densification of the composite (at least 92%). Hence, the influence of the microstructure could be neglected when tribologically comparing the different composites.

The blends were pre-compacted in steel dies (diameter: 8 mm) with a pressure of 990 MPa. Then, the pellets are

densified in a hot uniaxial press (with Al₂O₃ pistons) with an applied pressure of 264 MPa, temperature of 700°C, a heating and cooling rate of 20°C/min and a holding time of 2.5 hours.

After densification, all samples were ground under water rinsing with successive sandpaper grit sizes of 320, 600, 1000, 2500 grit and then polished in a three-stage process using diamond polishing suspensions in the steps 6 μm, 3 μm and finally 1 μm.

2.2 Numerical modeling

Before tribological testing of the samples commences, it is desirable to estimate the contact conditions occurring under static loading. It is important to know whether the contact is fully elastic or elasto-plastic as it might influence the lubrication mechanism of the CNP. Therefore, it is important to determine which normal forces are needed for the given tribological system in order to provide reasonable contact situations. In order to find the statistical parameters for the simulation, real surface data had been obtained by laser scanning microscopy (LEXT OLS4100 by Olympus) with a lateral resolution of 120 nm and a height resolution of 10 nm using a 50x objective. For the simulation, the surface data of the unreinforced composite and the counterpart, consisting of an Al₂O₃ ball with a diameter of 6 mm, are used. To find the corresponding statistical surface parameters, the spectral moments can be employed:

$$m_0 = \frac{1}{N} \sum_{n=1}^N (z)_n^2 \quad (1)$$

$$m_2 = \frac{1}{N} \sum_{n=1}^N \left(\frac{dz}{dx} \right)_n^2 \quad (2)$$

$$m_4 = \frac{1}{N} \sum_{n=1}^N \left(\frac{d^2z}{dx^2} \right)_n^2 \quad (3)$$

where N is the total number of data points on a surface and z is the distance from the mean height of the surface to the asperity peak. The derivatives are calculated by a central finite difference scheme. In this work, both surfaces exhibit non-isotropic roughness and thus they are meshed into 2-D individual rows and columns. Along each of these directions, moments are averaged arithmetically (m_0) and harmonically (m_2 & m_4) in principal directions defined by where m_2 is maximum and minimum. The following procedure is then used:

1. Find *one* set of two orthogonal directions which give $m_{2(min)}$ and $m_{2(max)}$. Ignore all other values and directions. Calculate m_2 by harmonic mean from $m_{2(min)}$ and $m_{2(max)}$.
2. In that *specific* directions set above, calculate $m_{4(1)}$ and $m_{4(2)}$ (regardless of whether they are maximum or minimum). Calculate m_4 by harmonic mean from $m_{4(1)}$ and $m_{4(2)}$.
3. In that *specific* directions set above, calculate $m_{0(1)}$ and $m_{0(2)}$ (regardless of whether they are maximum or minimum). Calculate m_0 by arithmetic mean from $m_{0(1)}$ and $m_{0(2)}$.

The radius of curvature, R , the areal asperity density, η , and the root mean square, σ , are then calculated according to the work by McCool [49] using spectral moments obtained from the above procedure:

$$\sigma = \sqrt{m_0} \quad (4)$$

$$\eta = \left(\frac{m_4}{m_2}\right) \cdot \left(\frac{1}{6\pi\sqrt{3}}\right) \quad (5)$$

$$R = 0.375 \cdot \left(\frac{\pi}{m_4}\right)^{0.5} \quad (6)$$

In addition, the standard deviation of the summit heights, σ_s , and the separation between the mean of the surface and summit surfaces, y_s , and the bandwidth parameter, α , are also calculated based upon:

$$\alpha = \frac{m_0 \cdot m_4}{m_2^2} \quad (7)$$

$$\sigma_s^2 = \left(1 - \frac{0.8968}{\alpha}\right) \cdot m_0 \quad (8)$$

$$y_s = \frac{4 \cdot \sqrt{m_0}}{\sqrt{\pi \cdot \alpha}} \quad (9)$$

The model used is shown in **Fig. 1**. The model depicts an Al_2O_3 hemisphere that is brought into contact with a composite (CNT reinforced nickel) substrate. The surfaces, which have non-isotropic roughness, are set in a non-conformal contact. The contact is assumed to deform elasto-plastically, where bulk deformation is included.

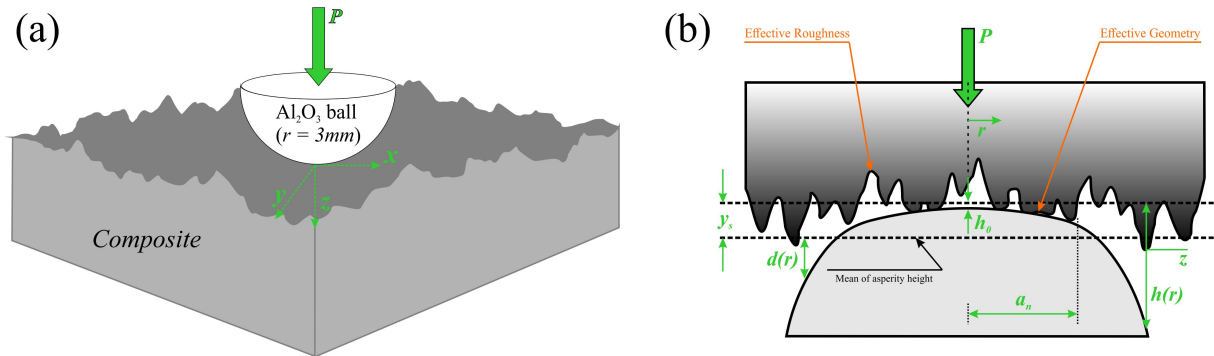


Fig. 1: (a) Schematic of contact between a rough hemisphere against a rough composite surface. (b) Contact model between an equivalent nominally flat rough surface against a smooth hemispherical-shaped counterpart.

The procedure for obtaining the clearance, h_0 (see **Fig. 1b**), and the final bulk deformation is outlined below:

- I. Get the bulk deformation δ caused by the load, P , according to:
 - (a) Obtain the critical load P_c that causes the onset of plasticity based on Green [51] (see Eq. 12 there);
 - (b) If $P < P_c$ use the Hertzian contact solution for the bulk deformation in a “pure” elastic state [52];
 - (c) If $P > P_c$ use the solution for the bulk deformation from [53] (see Fig. 5 there), and obtain the contact area from [56];
 - (d) superimpose the bulk deformation to the geometry of the sphere (see step IV below).

- II. Get the nominal pressure (p) and the real contact area (A_r) as a function of separation (h), as if the surfaces are both flat (conformal).
- III. Make p and A_r functions of that separation, h .
- IV. Assume (or “guess”) a clearance h_0 and form a function $h = h(r)$ that includes the bulk deformation.
- V. Integrate (i.e., sum) p and A_r over “rings” at r with a differential width Δr to obtain the load P as a function of clearance h_0 , and plot those results.
- VI. Find that clearance h_0 that corresponds to the applied experimental load P (0.1 or 8 N).
- VII. For that clearance, calculate the real area of contact (post processing).

2.3 Characterization methods

2.3.1 Tribological characterization

The tribological experiments are performed with two ball-on-disc tribometers (a nano and a microtribometer from CSM instruments). This allows to measure under significantly different loads and environmental conditions. In both cases the static counterpart consisted of an Al_2O_3 ball with a diameter of 6 mm (roughness $R_a = 22 \pm 7 \text{ nm}$). The test parameters for both tribometers are summarized in **Table 1**.

Table 1 – Test parameters of the tribological experiments.

	Test load [N]	Maximum speed [mm/s]	Stroke length [mm]	Temperature [°C]	Humidity [%]	Sliding distance [m]	Mode
Nanotribometer	0.1	1	0.6	25	4	0.72	Linear
Microtribometer	8	10	4	25	45	2.4	reciprocating

The choice of two different tribometers (working under different normal loads) is made according to the calculated contact conditions, which should be elastic and elasto-plastic (see section 3.1). Furthermore, the nanotribometer allows the systematic investigation of the lubrication activity at very low room humidity. Specifically, in the case of a full degradation of the CNPs towards graphite, it is expected that the lubricity will be severely hindered as a consequence of the shortage of water molecules that enhance the lubrication mechanism in graphite [54–56]. Thus, the reason for choosing two different relative humidities is to evaluate the lubrication behavior actively avoiding or allowing for a graphitic lubrication. All individual measurements have been repeated three times for statistical back-up. Consequently, the mean value including standard deviation is plotted for every investigated case. Al_2O_3 was selected as counterpart material because of its chemical inertness, low adhesion to the metallic matrix (compared to a metallic counterpart) and a much higher hardness compared to the composites. Due to these facts, wear of the alumina ball can be neglected and the focus can be put on the wear analysis of the composites.

2.3.2 Nanoparticle characterization

The structural state of the particles is surveyed by Raman spectroscopy. The data is acquired using an inVia Raman microscope (Renishaw) with an excitation wavelength of 532 nm (2.33 eV), a grating with 2400 lines per

mm, a 50X-objective (numerical aperture: 0.9), a spectral resolution of 1.2 1/cm, and a laser power of 0.2 mW. Visible excitation wavelengths in Raman spectroscopy are more sensitive (50 to 230 times for graphite and amorphous carbon, respectively) to coupled modes induced by sp^2 -carbon atoms than for sp^3 [57,58]. Thus, NDs (sp^3 -hybridization) Raman signal is weaker and might not be detected for the initial state. However, if a transformation of ND towards graphitic structures occurs, this could be easily observed as a consequence of the appearance of the sp^2 characteristic D and G bands. All Raman spectra were recorded three times with an acquisition time of 10 s to eliminate cosmic rays and to improve the signal-to-noise ratio. Additionally, a linear baseline subtraction and intensity normalization were performed for all spectra. To identify peak positions of the data, fitting with Lorentz functions was performed for all data [59]. The distribution of the particles in the matrix was analyzed using a light microscope (BX 60, Olympus).

2.3.3 Microstructural characterization

The mean grain size of the matrix after sintering determined by EBSD with an EDAX TSL detector incorporated in the dual beam microscope. The scanned area is of $250 \times 250 \mu\text{m}^2$ applying an accelerating voltage of 20 kV, a current of 22 nA, and a step size of 0.3 μm . For the analysis, a grain is defined as at least two adjacent points with a maximum misorientation of 5° , beyond which a grain boundary is determined. The acquired raw data was post-processed using confidence index (CI) standardization, followed by the removal of points with CI below 0.1. The grains intersecting the scan window were excluded from the analysis.

2.3.4 Wear track and surface roughness analysis

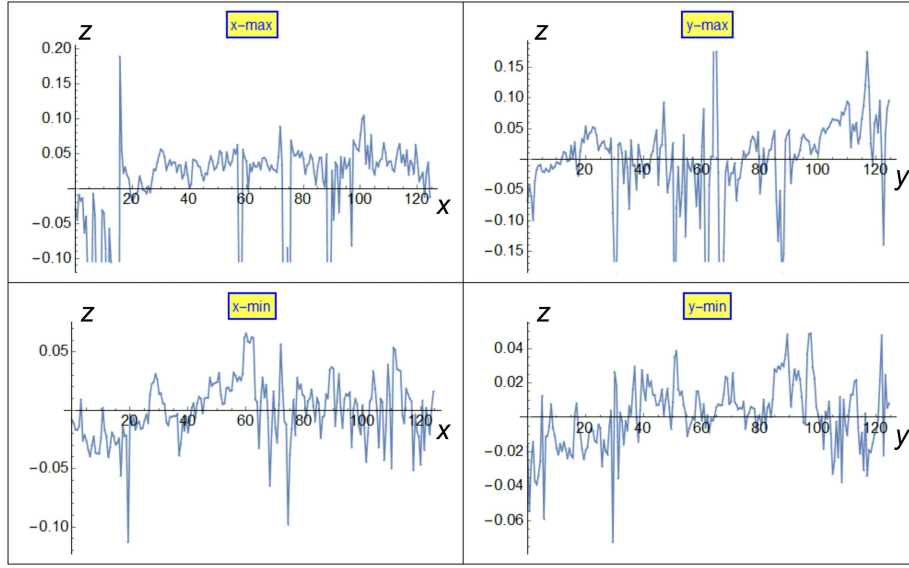
Before the tribological measurements, the surface roughness is determined for each sample using the laser scanning microscope. After the experiments, the wear tracks are analyzed using a dual beam focused ion beam/field emission scanning electron microscopy (FIB/FE-SEM) workstation (FEI Helios NanoLab 600) with a voltage of 5 kV and 1.4 nA of current. Finally, also energy dispersive X-ray spectroscopy (EDS) is performed for the wear tracks using a voltage of 5 kV and a current of 22 nA. The analysis of the sub-surface is performed on a transmission electron microscope (TEM) JEOL JEM 2010 working at 200 kV.

3 Results and discussion

3.1 Contact mechanics modeling results

The roughness of the composite surface varies greatly in various radial directions, requiring the three-step special procedure to calculate the effective moments as detailed in section 2.2. The surfaces roughness is digitized by a resolution of 0.125 μm . **Fig. 2a** shows the roughness of the composite while **Fig. 2b** shows the roughness of the ball in the corresponding $m_{2(min)}$ and $m_{2(max)}$ directions.

(a) composite



(b) counterpart

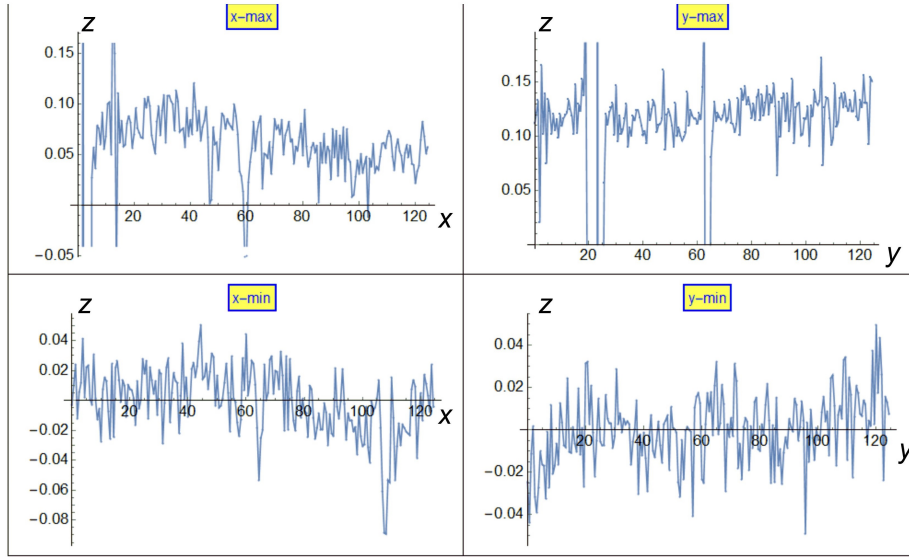


Fig. 2: Roughness line profiles in the maximum and minimum directions of (a) the composite, (b) the counterpart. All dimensions are in μm . The width shown corresponds in all cases to $120 \mu\text{m}$.

By the procedure outlined above and using **Eqs. (1-9)**, the descriptive values of the surfaces are obtained. Following the definition given by Greenwood and Williamson [44] the plasticity index is:

$$\psi = \left(\frac{E^*}{H}\right) \cdot \sqrt{\frac{\sigma}{R}} = 8.8 \quad (10)$$

That value indicates that surface asperities would clearly undergo plastic deformation. The next step is to determine whether the bulk remains elastic (see step I above). Using Hertzian theory as outlined by Johnson [60], the bulk deformation is shown in **Fig. 3**. The solution is obtained piecewise with the vertical line marking

the radial position where to the left of it there is complete contact between the surfaces, while to the right the ball and the composite are separated. [Note that rough surfaces contact still takes place throughout, i.e., in both regions].

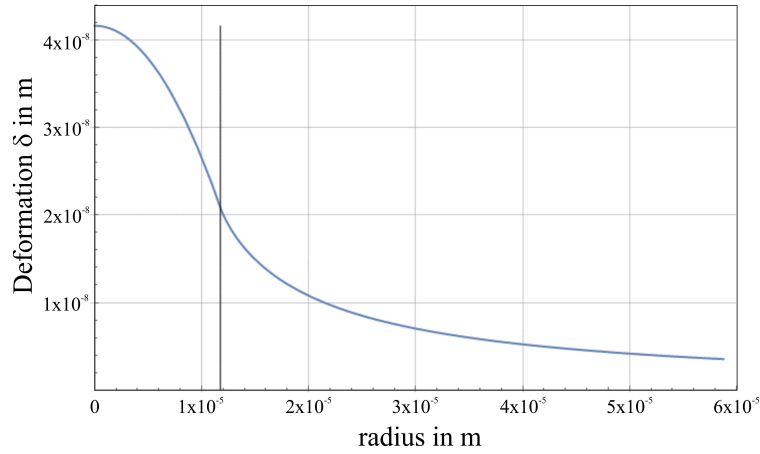


Fig. 3: Substrate deformation under a load of 0.1 N. The vertical line separates complete contact (left) and non-contact (right).

The maximum deformation under the action of the load of 0.1 N is at the origin giving $\delta = 46$ nm, whereas the critical value at the onset of plasticity is 152 nm [60]. Likewise, the critical value of the load that would cause plasticity in the bulk is 0.6 N (using [51]). Evidently, for that load the bulk deforms entirely elastically, whereas the asperities will deform in the elasto-plastic regime (because the plasticity index is 8.8). This fulfills step I above. Now the Jackson-Green (J-G) model [50,61] is employed for the elasto-plastic asperity contact. The results are shown in **Fig. 4 a & b** (the Greenwood-Williamson (G-W) and the corrected Kogut-Etsion (K-E) models are shown for reference only). This is in accordance with steps II and III above.

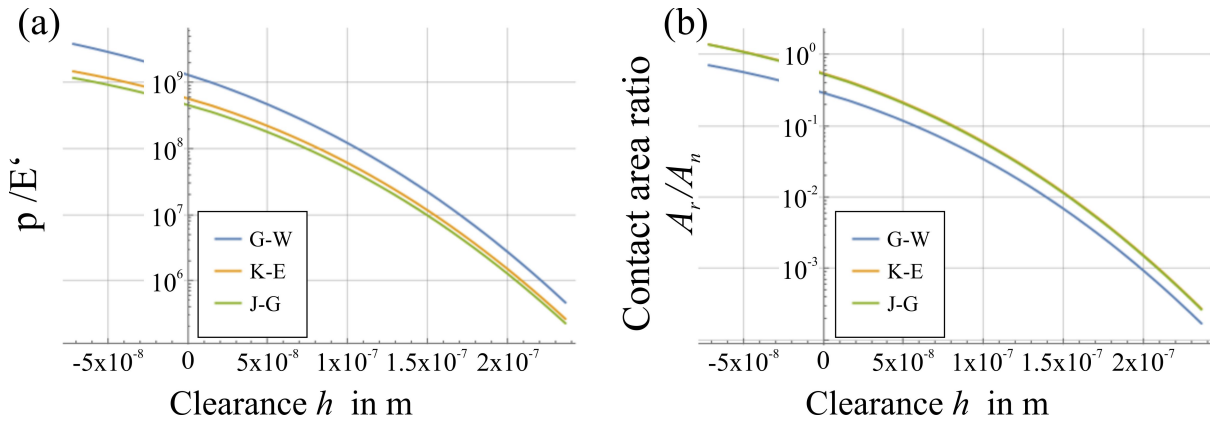


Fig. 4: (a) effective pressure p divided by reduced modulus E' vs. the clearance, and (b) Contact area ratio vs. the clearance

Steps IV and V above are subsequently performed. For brevity details are omitted but the outcome is shown in **Fig. 5**. Then, in step VI, the particular clearance h_0 that corresponds to the applied experimental load is found. Hence, entering **Fig. 5** with a load of 0.1 N, the clearance is found to be $h_0 = 41$ nm. Superimposing the asperities deformation along with the bulk deformation (attributing the entire latter deformation to the ball) gives the final flattened shape of the ball shown in **Fig. 6a**, while the pressure distribution at the contact is shown in

Fig. 6b. It is evident that also the pressure distribution is flattened (compared to the Hertzian parabolic shape), where it is nearly constant in the full contact region, but it drops outside of that region.

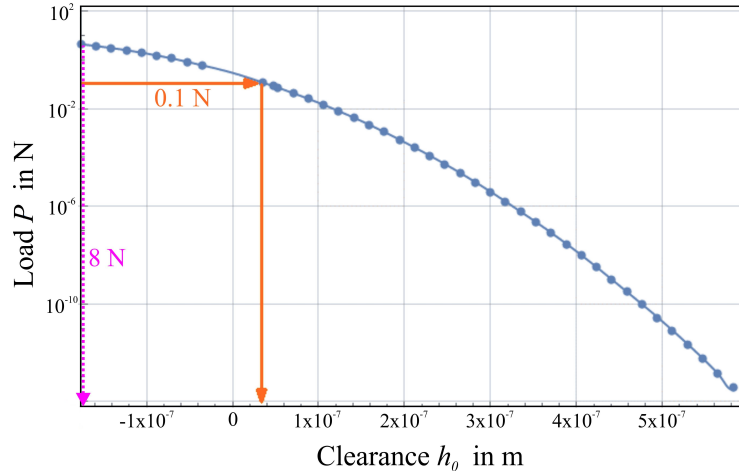


Fig. 5: Contact load as a function of the clearance h_0 between the contact pair. The arrows indicate both experimental loads investigated in this report.

The real area of contact is now finally evaluated in the two regions using the J-G model (with the information given in **Fig. 3**). In the region where the ball bulk is in contact with the composite (that is in the range $0 < r < a_0 = 11.74 \mu\text{m}$, where a_0 is identified by the vertical lines in **Fig. 3 and 6**) the real contact area is $3.67 \times 10^{-11} \text{ m}^2$, and the asperities contact outside that region (where $r > a_0 = 11.74 \text{ nm}$) result in a contact area of $5.57 \times 10^{-11} \text{ m}^2$. The total real contact area is the sum of these, giving $9.25 \times 10^{-11} \text{ m}^2$.

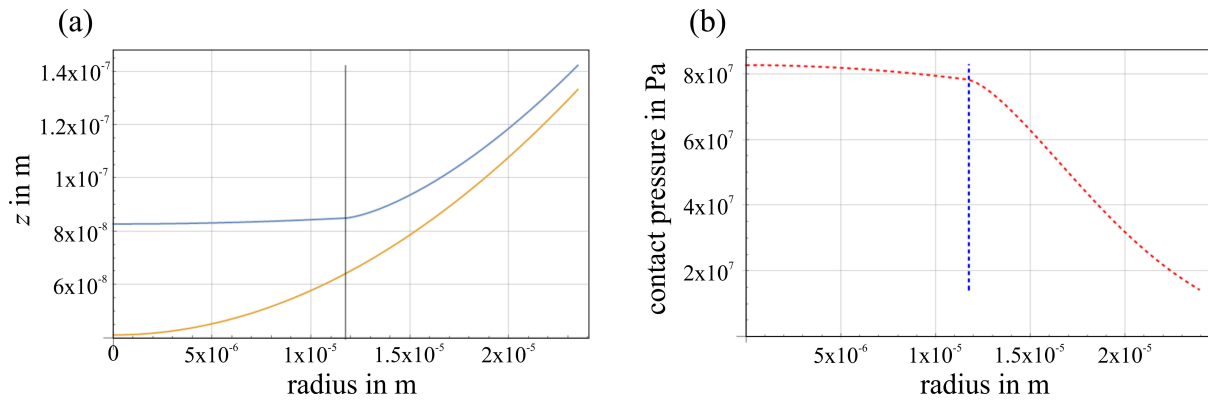


Fig. 6: (a) Deformation profile of the surface (blue) and the original surface profile (orange). (b) Contact pressure distribution throughout the counterpart radius.

For the case when the load is 8N , it is apparent from **Fig. 5** that a negative value would be anticipated for h_0 . That indicates that the contact is heavily loaded making rough surfaces analysis moot. In this case, it can be assumed that all asperities have been heavily and severely (plastically) deformed and the entire contact degenerates into a single elastoplastic spherical contact. The J-G model [50,61] is readily used to estimate the contact parameters. First the normalized load is calculated $P^* = P/P_c$, where P_c had already been obtained previously ($P_c = 0.6 \text{ N}$). Using the load of 8N , gives $P^* = 8/0.6 = 13.3$. Reverse-solving for the normalized interference (from J-G [50,61]), gives a non-dimensional interference $\omega^* = 6$. It is now straightforward to calculate the real area of contact from the said reference, where first the nondimensional value is calculated, A^*

$= A/A_c = 7.15$. Then, the critical area of contact is calculated, $A_c = 1.43 \times 10^{-9} \text{ m}^2$, to finally obtain the real area of contact $A = 1.02 \times 10^{-8} \text{ m}^2$. This value is two orders of magnitude larger than for that of the previous case (when the load is 0.1 N).

Based on these modeling results, the elastic and elasto-plastic contact regime is covered by choosing normal forces of 0.1 and 8 N. The lower load resides below the calculated critical elastic-plastic transition load, whereas the higher resides clearly well above it.

3.2 Initial state characterization

After surface preparation, the distribution of the reinforcement phases was analyzed by light microscopy. In **Fig. 7**, the distribution of the CNT agglomerates (dark regions) is shown as a function of the volume fraction in the composite. Earlier studies have shown, that the dark regions can directly be assigned to CNT agglomerates [42]. As expected, the amount of agglomerates is gradually increasing with higher volume concentration. However, the distribution of the particles seems to be unaffected by the amount of reinforcement phase, thus a homogeneous distribution of smaller and larger agglomerates within a constant size range is achieved in all cases. This is also the case for the composites reinforced with OLC and nD (the depicted micrographs are representative for all composites).

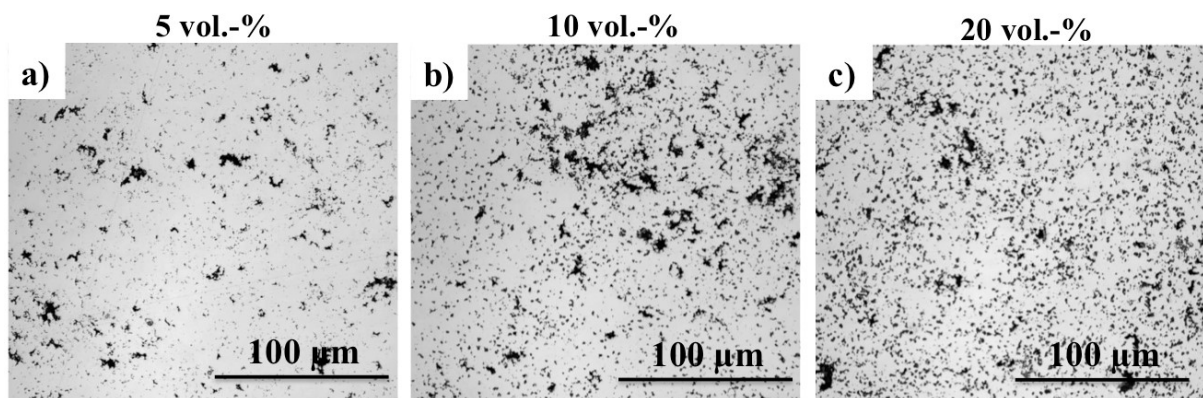


Fig 7: CNT agglomerates (dark regions) distribution in the nickel matrix composites for a) 5 vol.-%, b) 10 vol.-% and c) 20 vol.-%. The distributions are also representative of the composites reinforced with OLC or nD.

The surfaces were also evaluated with regards to their initial surface roughness after preparation by white light interferometry. In **Table 2**, the mean values and standard deviation of the surface roughness R_a for all composites is presented.

Table 2 - Mean values and standard deviation of the surface roughness from the as-prepared surfaces of the composites with 5, 10 and 20 vol.-% concentrations of CNT, OLC or nD as reinforcement particles.

Sample		R _a (nm)
Unreinforced Ni		2.4 ± 0.1
CNT	5 vol.-%	13.6 ± 2.6
	10 vol.-%	19.1 ± 5.5
	20 vol.-%	38.6 ± 7.4
OLC	5 vol.-%	14.2 ± 6.0
	10 vol.-%	57.6 ± 3.7
	20 vol.-%	122.0 ± 39.5
nD	5 vol.-%	9.0 ± 5.5
	10 vol.-%	73.1 ± 16.2
	20 vol.-%	141.7 ± 19.5

The surface roughness of the composites is gradually increasing with the amount of reinforcement phase even though the surface preparation was the same. In addition, the surface roughness of nD and OLC reinforced composites is significantly higher for 10 and 20 vol.-% compared to the CNT reinforced composites. For one part, this is a consequence of the different adhesion to a nickel matrix of both carbon hybridizations studied, where the adhesion of sp² carbon is higher than in case of sp³ hybridized carbons [62]. Thus, the nD particles are removed easily from cavities of the surface during the sanding and polishing process. Naturally, higher particle concentrations result in a larger amount of cavities exposed to the surface, hence deriving in a higher resulting surface porosity and accordingly, a higher roughness. A higher porosity of the samples before surface preparation can be excluded as the relative densities of all composites are determined and reach a value of around 92 %. Furthermore, CNT composites show lower surface roughness, as they are more likely to form mechanically interlocked agglomerates within the cavities due to their high aspect ratio. Thus, it is more difficult to remove them during the surface preparation process, as opposed to both, OLC or nD.

The reference and the composites were further analyzed by EBSD in order to evaluate the resulting microstructure after densification. No change in the mean grain size or texture was observed as a function of the different particle volume contents or type. The observed behavior can be explained with the chosen sintering parameters, not allowing the grains to efficiently grow. Thus, the boundary pinning generated by the particles is marginally developed. This becomes clear when comparing the mean grain size of the unreinforced nickel of 7 ± 2 μm with the mean grain size of all the composites of 3 ± 1 μm. Compared to a previous report, this reduction in mean grain size is not distinctive [42].

3.3 Frictional behavior

In **Fig. 8** the measured evolution of the friction coefficients (COF) for 5, 10 and 20 vol.-% of nD, OLC and CNT are shown for 0.1 N of load and a relative humidity of 4 %. The COF of the reference measurement increases during the first 100 cycles from 0.4 to 0.47 (plotted in **Fig. 8 a, b and c** for better clarity). From there on, the COF drops down to 0.39 during the next 500 sliding cycles, finally reaching steady state. This behavior is well-known for this contact situation and has been extensively discussed by Blau et al. [63]. The increasing COF for the first 100 cycles is explained with an increasing real contact area due to the wearing off of intrinsic asperities

and an increment of the indentation depth of the ball into the substrate. Subsequently, the contact starts to reach a higher surface conformity and smoothing occurs, leading to a frictional reduction. The obtained steady-state reference COF of 0.39 is in agreement with the value reported in the literature [16,64]. Looking at the frictional behavior of the nD (**Fig. 8a**) or OLC (**Fig. 8b**) reinforced samples, a similar evolution of the COF to that of the reference can be observed. Considering the given curve dispersion, a change in volume fraction of both particle types leads to no significant change in the COF. This supports the assumption that the frictional behavior of these samples is dominated either by the direct contact of the counterpart with the nickel matrix or a tribologically generated oxide layer. This could be traced back to the fact that large quantities of the particles have been removed from the cavities of the surface during the surface finishing process. However, the mean COF value of the CNT reinforced samples (**Fig. 8c**) clearly decreases as a function of their volume fraction. This is also related to the different surface roughness and to the different particle size and morphology. As the roughness of nD and OLC containing samples highly exceeds the mean particle size of the spherical particles (4-10 nm), it is highly likely that the particles cannot separate the two contacting surfaces any longer, thus avoiding an efficient lubrication activity [39]. It is also likely that the formation of wear particles larger than the carbon nanoparticles or the formation of an oxide layer would explain the observed behavior.

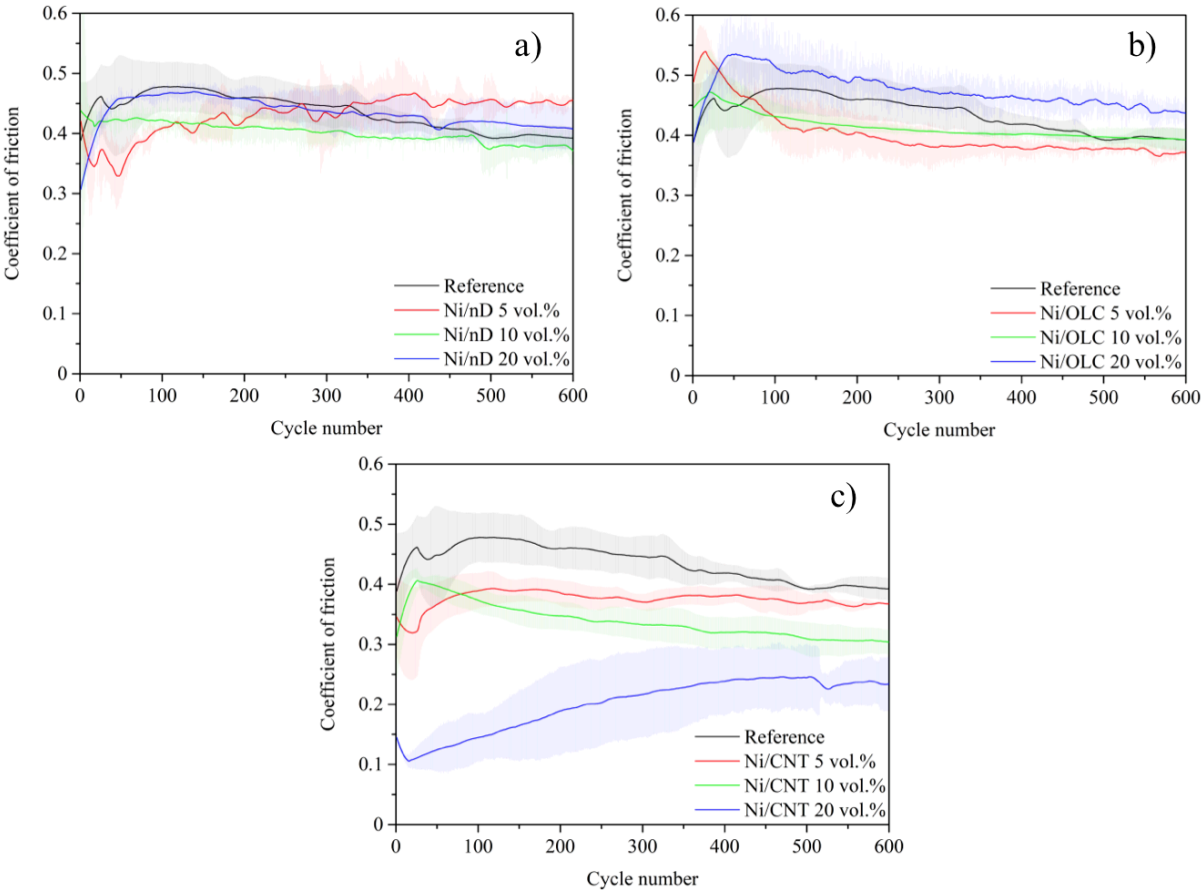


Fig 8: Evolution of the COF for unreinforced nickel (Ref) and 5, 10 and 20 vol.-% of a) nD, b) OLC and c) CNT in a nickel matrix. The experiments were conducted using 0.1 N of normal load, a relative humidity of 4 % and a temperature of 25 °C.

In contrast to that, CNT provide a large aspect ratio (diameter of 5-20 nm with a length of 2-10 μm), which enables them to be dragged inside of the direct tribological contact zone thus lubricating the contact [30,65]. In previous studies, it was observed, that the tribological behavior of the composites is dominated by the presence

or absence of CNT [16]. Thus, it is reasonable, that the COF is decreasing with increasing volume content of CNT. Furthermore, the COF for 20 vol.-% of CNT is increasing from 0.1 to 0.2 during running in. This could be explained with the formation of wear particles or oxide layers during the experiment, hindering CNT in their ability to slide or roll. Furthermore, although the contact pressure is chosen in order to avoid a structural delamination of the CNT towards graphite, it cannot be excluded. This is because higher contact pressures could be reached between individual asperities of the contacting surfaces. In this case, CNT would change its lubrication mechanism from a sliding or rolling movement at the beginning (COF = 0.1) to a more graphite like lubrication in the steady state regime (COF = 0.2). However, as the relative humidity of the experiment is only 4 %, a straight graphitic lubrication can be excluded. Considering, that pristine CNT are included in the matrix material, it appears reasonable, that a mixture of pristine CNT and delaminated CNT dominates the frictional behavior under steady state conditions. Additionally, a low relative humidity could slow down the running-in process due to a retarded formation of an oxide layer, which would explain a lower COF of CNT at the beginning of the measurement. However, this can be excluded as this effect should also be observed for all the other sample types, which is not the case. Therefore, a possible retarded surfaces oxidation could only be associated with the CNT particles or tribofilm and not the relative humidity. Raman spectroscopy, SEM and EDS analysis of the according wear tracks will investigate these assumptions further.

The investigation of the influence of the particle concentration on the friction coefficient has shown, that an enhanced lubrication can be reached with higher volume concentrations (for CNT). Thus, for the experiments with 8 N of normal load only the samples with 20 vol.-% of reinforcement phase were measured. In **Fig. 9**, the evolution of the COF for the reference and the three particle types is plotted.

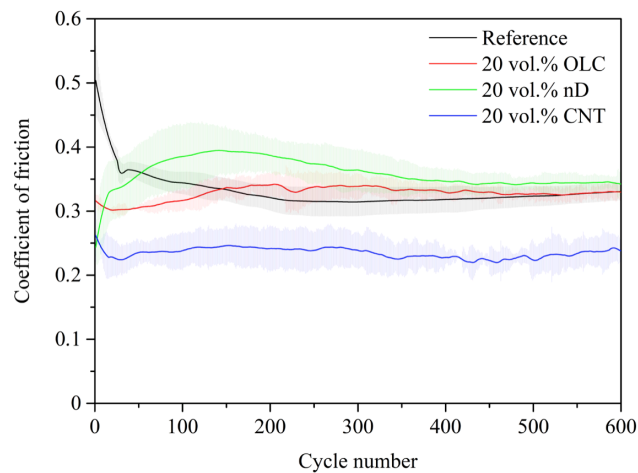


Fig 9: Evolution of the COF for unreinforced nickel (Ref) and 20 vol.-% of OLC, nD and CNT in a nickel matrix. The experiments were conducted using 8 N of normal load, a relative humidity of 45 % and a temperature of 25 °C.

For this contact situation, a similar behavior compared to the 0.1 N load is noticed. In case of the reference, The COF drops from 0.5 to 0.35 during the first 40 sliding cycles. After this, it stabilizes to a value of 0.35 and thus reaches steady-state condition. This type of COF evolution is also already well-known and typical for high contact pressures on metallic surfaces as reported by Blau et al. [63].

Although showing a slightly different run-in process, the OLC or nD reinforced samples stabilize towards the same COF value as the reference under steady state condition. The slight differences during the run-in process might arise from the initially high roughness of the composites, also resulting in a higher standard deviation. The

standard deviation becomes smaller as soon as the system undergoes the transition towards steady-state condition, which could be explained with the removal of the initially present large surface asperities and thus the reach of surface conformity. No lubrication is observed for both types of particles. In contrast to the 0.1 N measurements, this cannot be explained with the absence of particles anymore. In case of higher contact pressures and a plastic deformation of the material, much higher wear is expected also revealing particle agglomerates that are encapsulated in the nickel matrix below the surface. Considering the behavior of the CNT reinforced samples, a constant lubrication effect is noticeable. However, the COF is not reaching values below 0.2 as it was observed for the 0.1 N load measurements. This might be because of a faster degradation process of the CNT due to a much higher contact pressure and a quicker running in process due to surface oxidation (which is promoted by the higher relative humidity) in combination with the much higher contact pressure. The formation of a lubricating absorbed water film can be excluded, since no lubrication is observed for nD or OLC reinforced composites. In contrast, lubrication does not vanish for CNT reinforced composites and is also present under steady state conditions.

3.4 Wear behavior at low load (0.1 N)

In order to achieve a better understanding of the acting tribo-mechanisms, the wear-tracks have to be analyzed in more detail. **Fig. 10** depicts SEM micrographs of the wear tracks of the reference and of the samples reinforced with 20 vol.-% of CNP for the 0.1 N load measurements.

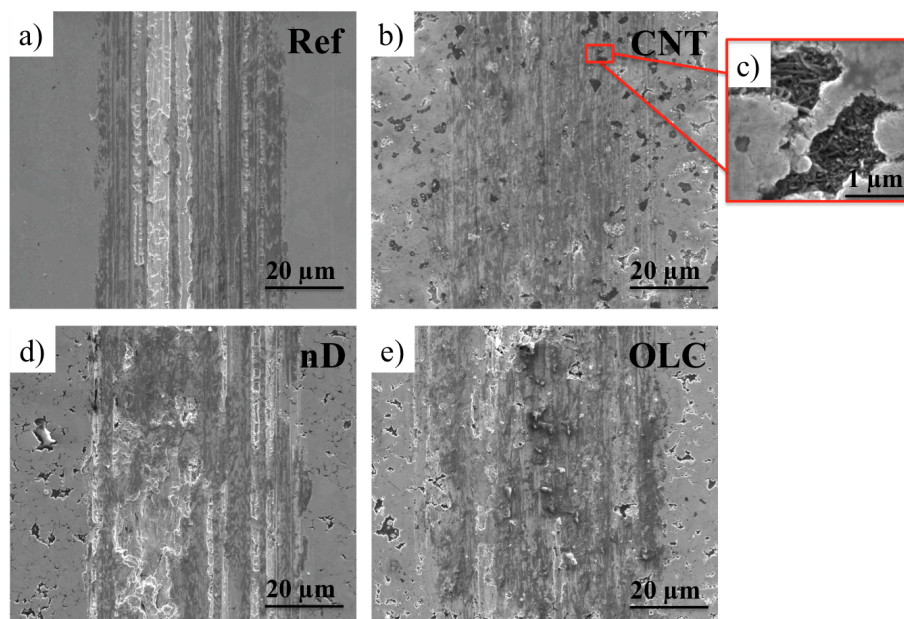


Fig 10: Wear tracks for 0.1 N of normal load under 4 % of relative humidity in case of a) the unreinforced reference and composites reinforced with 20 vol.-% of b) CNT, d) nD and e) OLC. A surface cavity of the CNT reinforced sample is depicted in c).

The reference clearly shows signs of abrasive wear with plowing being the dominant wear mechanism (**Fig. 10a**). A similar behavior is observed for the nD and OLC reinforced composites (**Fig. 10 d** and **e**). However, in case of the CNT reinforced samples, the wear mechanisms seem to differ (**Fig. 10 b**). Although a direct contact between the two surfaces is not fully prohibited by the CNT, only mild wear is occurring. As already described

in the discussion of the friction coefficient, this is explained with the large aspect ratio of CNT, which enables them to be dragged inside of the direct tribological contact zone thus reducing the direct contact of the alumina ball with the nickel matrix. In contrast to the nD and OLC reinforced samples, CNT agglomerates (dark regions) can still be observed within the wear track, demonstrating, that less plastic deformation or oxidation of the surrounding nickel matrix has occurred. Furthermore, in **Fig. 10 c**, CNT are found inside the surface cavities within the direct contact area. In this case, the formed tribolayer might consist out of nanocrystalline graphite layers, which were formed by delamination of CNT as they lubricate the contact. The oxidation behavior was further analyzed by EDS-mapping of oxygen in **Fig. 11**.

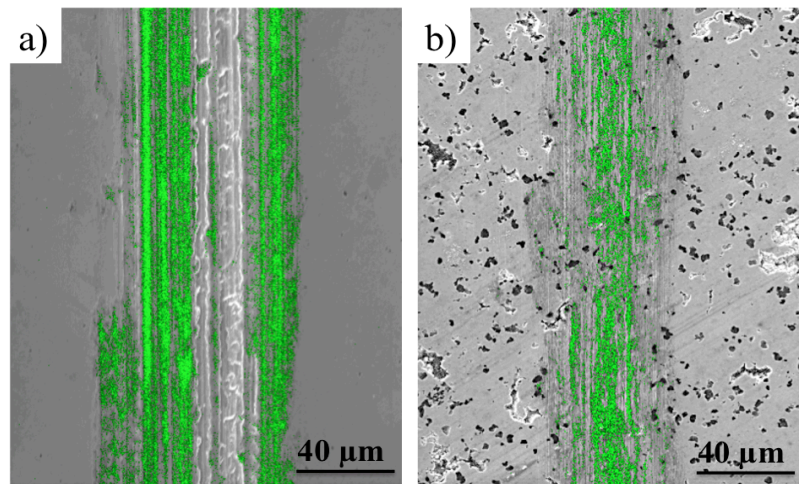


Fig 11: EDS maps of oxygen (marked in the color green), superimposed with SEM images of the wear tracks for 0.1 N of normal load under 4 % of relative humidity in case of a) the unreinforced reference and b) the composite reinforced with 20 vol.-% of CNT.

The wear track of the unreinforced reference (**Fig. 11a**) shows large areas with high oxygen content, which are randomly distributed within the wear track. This could be explained with the ongoing plowing mechanism, which stochastically reorders oxides and bare metal. With the wear mechanism of nD and OLC reinforced samples being similar to those of the reference, the depicted EDS-map is representative also for those samples. However, in case of CNT reinforced samples (**Fig. 11b**), the EDS-map clearly shows, that the wear track is less oxidized. These observation correlates well with the wear mechanism, as a stronger formation of an oxide layer and the development of oxidic wear particles during the experiment would result in a more pronounced abrasive component. Considering the evolution of the COF, the formation of a more pronounced oxide layer or oxidic wear particles that are embedded in the surface cavities in case of the reference, nD and OLC reinforced samples leads to the stabilization of the COF, finally reaching similar values in the steady state regime. With the CNT-reinforced samples showing less oxidation and a lower COF, it appears reasonable that the COF can still be dominated by the CNT instead of oxidic wear particles.

3.5 Wear behavior at high load (8 N)

Regarding the experiments with higher contact pressure (8 N), a different wear behavior is found, as can be seen in **Fig. 12**. As for the measurements with 0.1 N load, plowing can be identified as dominant wear mechanism for the reference. A slightly darker color of the wear track leads to the assumption that an oxide layer has formed

during the experiment, which will be further evaluated by EDS mapping and Raman spectroscopy in the following sections (**Fig. 12a**).

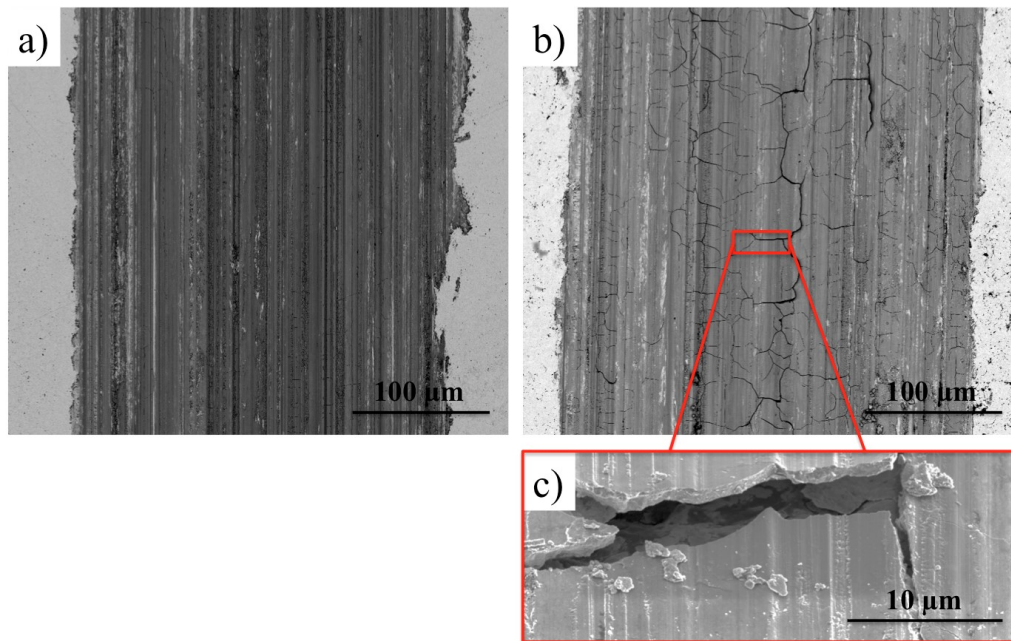


Fig 12: Wear tracks for 8 N of normal load under 45 % of relative humidity in case of a) the pure Ni reference and b) a composite reinforced with 20 vol.-% of CNT. The formation of loosely connected sheets on the surface of the wear track is depicted in a higher magnification in c).

The wear track of the CNT reinforced sample in **Fig. 12b**) is representative for nD and OLC reinforced samples as well. Beside the occurrence of abrasive wear, a distinctive formation of cracks all over the wear track is obvious. When looking at these cracks in more detail in **Fig. 12c**), it is found, that the cracks occur within a formed surface layer, resulting in the formation of independent surface sheets. The sheets are only loosely attached to the surface as large gaps between the surface and the sheets are present. Due to the high contact pressures, the surface layer might form by densification of wear particles, Ni and CNP. This is reasonable, as for the provided high contact pressure and the resulting wear of the surface, the CNP situated below the initial surface are brought into the tribological contact region. Finally, they are mixed with oxidic wear particles and Ni in a stochastic manner, all being compacted to form the observed surface layer. It can thus be concluded that, although the frictional behavior of the composites is obviously differing (see **Fig. 9**), the wear behavior under high contact pressure and medium relative humidity can be quite similar. The explanation on the formation of the observed surface sheets will be further verified using EDS mappings and TEM analysis in the following sections. In **Fig. 13**, the wear tracks are characterized by EDS-mapping in order to analyze the oxygen and carbon distribution.

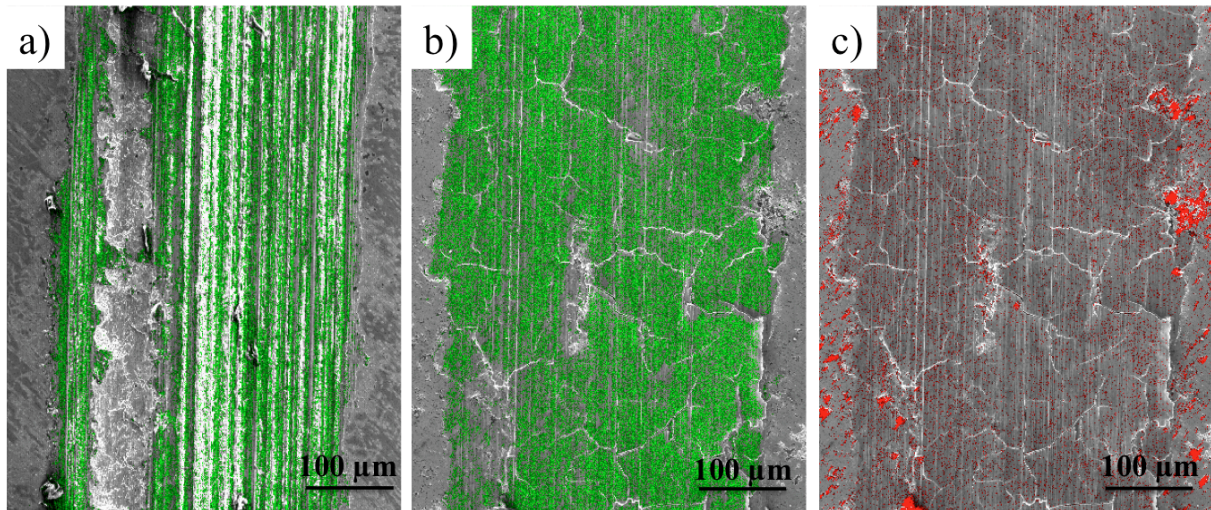


Fig 13: EDS maps of oxygen (marked in the color green), superimposed with SEM images of the wear tracks for 8 N of normal load under 45 % of relative humidity in case of a) the unreinforced reference and b) the composite reinforced with 20 vol.-% of CNT. In c), an EDS map of the carbon distribution (marked in the color red) of the wear track of the composite reinforced with 20 vol.-% of CNT is depicted.

The oxidation behavior of the reference wear track (**Fig. 13a**) has not significantly changed compared to the 0.1 N measurements. Still, the plowing mechanism reorders oxides and bare metal in a stochastic manner. In contrast to that, the formed layer, or individual sheets of the composite wear tracks show a homogeneous distribution of oxygen all over the wear track (**Fig. 13b**). This verifies that the formed sheets in fact consist of compacted oxidic wear particles. However, also carbon is homogeneously integrated into the surface sheets. Although the two originally contacting surfaces obviously cannot be separated anymore by CNP for high contact pressures (due to the formation of the surface layer), the lubrication effect is still active for CNT reinforced composites. Considering the gap between the sheets and the substrate in **Fig. 12c**, the cracking of the layer would allow the sheets to freely move during the tribological contact. Thus, it is reasonable, that the sheets could be separated from each other and from the substrate by the homogeneously distributed CNP. In fact, a frictional reduction in case of CNT reinforced composites is observed in **Fig. 9**, which could be explained with the larger size and morphology of CNT, compared to nD or OLC [65]. Due to the large aspect ratio, CNT could be dragged into the direct tribological contact, providing a sliding and/or rolling movement or delaminate and form graphitic structures thus lubricating the system [30].

A material transfer from the composite surface to the alumina ball has also been noticed for the high contact pressure experiments, vouching for a low adhesion of the surface sheets to the substrate. Thus, to extend the understanding of the composition of these sheets, a microstructural analysis with higher resolution is needed. **Fig. 14** shows a TEM foil obtained from one of the sheets. It is observed that the sheet is of nanocrystalline nature and is composed of an intermixing of three different phases. It is predominantly composed of NiO, but traces of Ni and C are detected, verifying the explanations from above. As already mentioned, it can be interpreted that the ploughing mechanism acts as driving force for the formation of these multiphase plates. Furthermore, the high contact pressure applied would severely deform the microstructure of the sheet, inducing dynamic recrystallization and strongly reducing the grain size.

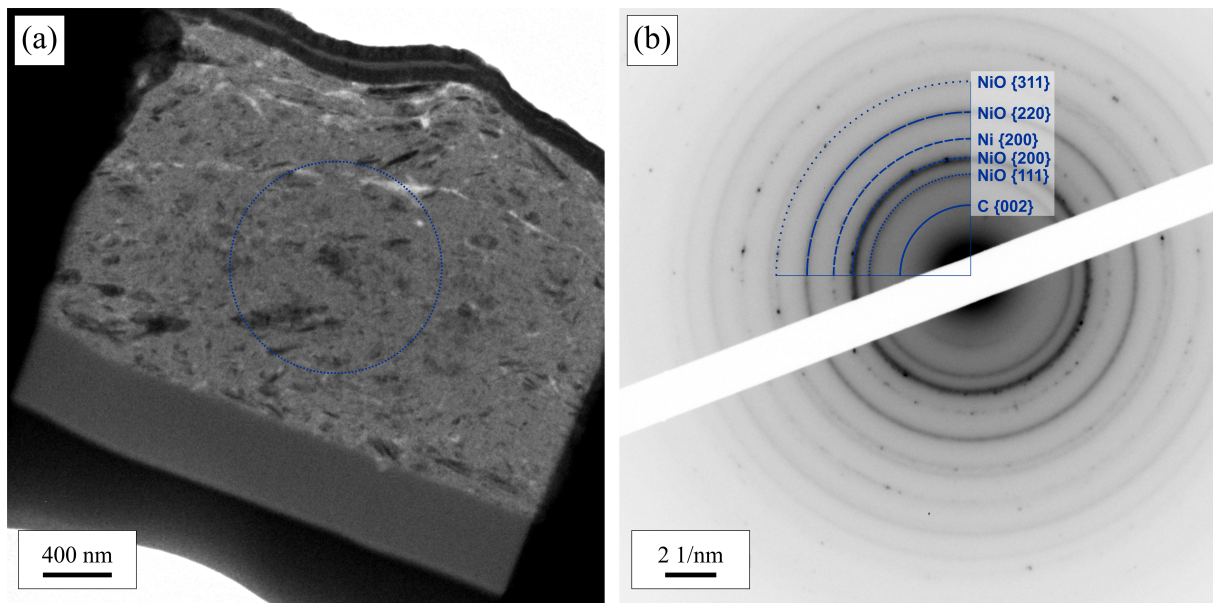


Fig 14: (a) Transmission electron micrograph of a foil obtained from the sheet observed in the Ni/CNT 20 vol.% samples tested with 8 N. The blue circle denotes the region where selected area electron diffraction was performed. (b) SAED pattern of the sample, where three different phases are identified (NiO, Ni and C).

Regarding the carbon signal observed in **Fig 14b**, it is not possible to precisely determine which morphology it would have. However, it can be unequivocally be related to carbon domains with a graphitic structure. A hypothesis for the formation of these sheets in case of the composite samples is the presence of carbon, which could act as a binder for the formed oxidic wear particles, allowing the formation of densified, but cracked sheets. However, an efficient lubrication is only given for CNT. The conclusion is therefore again fortified, that because of their larger size and high aspect ratio, CNT are able to separate the formed sheets and enable them to slide on each other and on the substrate. As nanocrystalline graphite is present in the sheets of all the CNP reinforced composites, it seems not to affect the COF significantly or the formed graphite flakes are too small to efficiently slide upon each other. Hence, lubrication is most likely based on sliding and/or rolling of CNT between the individual sheets.

3.6 Solid lubricant structural integrity assessment

The Raman spectra of the initial state CNP are shown in **Fig. 15** and will be used as reference state in the analysis of the structural integrity of the solid lubricant.

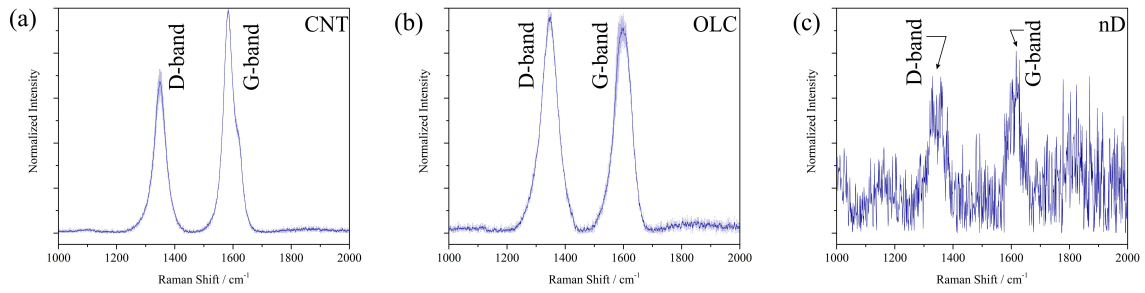


Fig 15: Raman spectra of the initial state of (a) CNT, (b) OLC and (c) nD. The two main bands (G and D) of sp^2 carbon are identified in the figure

It is observed that all type of particles show a seemingly high structural quality in their initial state. It is worth noting that the homogeneity in the features is remarkable, as interpreted from the small standard deviation bars in the plots of the CNT and OLC particles. In the nD case, the signal-to-noise ratio is significant, as a result from the measurement of these particles with visible light excitation. **Fig. 16** presents the Raman spectra acquired from the wear tracks for each sample type at different test loads and their corresponding relative humidity.

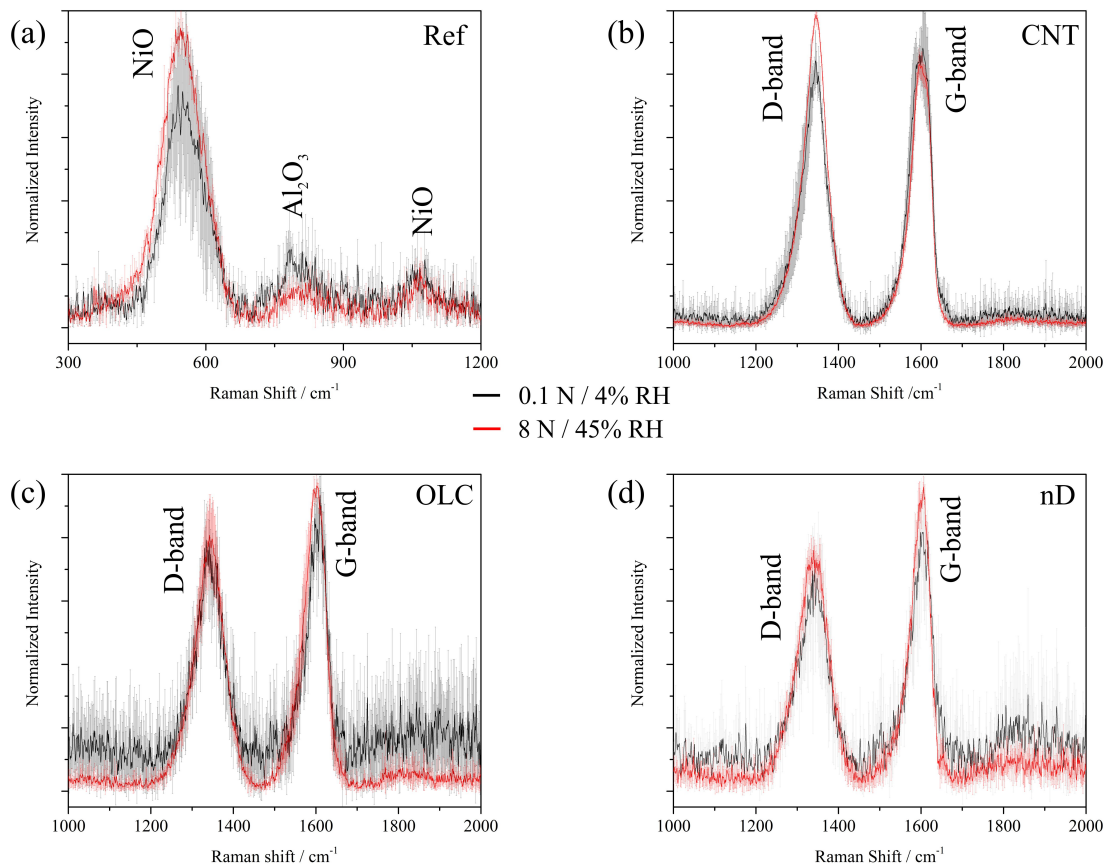


Fig 16: Raman spectra of the wear tracks of (a) reference, (b) CNT, (c) OLC and (d) nD samples. All relevant indexed bands are identified in each figure. The red and black plots correspond in all cases to 100 mN/ 4% relative humidity and 8 N/ 45% relative humidity, respectively.

The reference sample shows the characteristic bands of NiO in both tested loads (**Fig. 16a**). Furthermore, the signal corresponding to Al₂O₃ is a consequence of material transfer from the counterpart during the experiment. As opposed to the reference case, all particle types show no detectable oxide peaks in the Raman characterization, likely as a consequence of the strong presence of carbon in the wear track, reducing to some extent the detection of oxides. However, as shown in the section 3.4, oxide is indeed present in all cases. In the case of the CNT sample, there are no pronounced differences for both loads (**Fig. 16b**). When compared to the initial state of the CNTs (shown in **Fig. 15a**), the degradation is evident from the analysis of the intensity ratios and peak position, which is in agreement with the observations presented in Scharf et al. [30]. Specifically, the initial state CNTs have an I_D/I_G ratio of 0.68 and a G peak position of 1585.3 cm⁻¹, which correspond to CNTs with high degree of crystallinity. On the other hand, the post-test CNTs present an I_D/I_G ratio of 0.96 and 1.19 and a G peak position of 1603 and 1595 cm⁻¹, for 100 mN and 8 N respectively. The increment of the intensity ratio and the upshifting of the G band position vouch for a degradation of the CNTs [66] during the tribological contact, forming a lubricating nanocrystalline graphitic tribolayer, as already reported [30]. Regarding the OLC sample, the changes in the structural integrity of the particles is not as marked as in the CNT case (**Fig. 16c**), probably due to their inability to be effectively brought into contact during the test. This is supported by the values of the I_D/I_G ratio, which shows a change from 1.05 in the initial state (as observed from **Fig. 15b**) to 0.88 and 0.85 in the 100 mN and 8 N tests, respectively. Interestingly, the nD sample show strong resonance of the sp² carbon bands (**Fig. 16d**), which are theoretically present in very low volume fractions in the predominantly sp³ nanodiamond (as a result of the synthesis by detonation) [23,67]. The observation of these bands is explained by the difference in the behavior of both hybridization states to the excitation with visible light. It has been reported that the sp² domains are up to 230 times more sensitive to visible light excitation than those with sp³ hybridization, thus vanishing them in the background noise [57,58]. In any case, when compared to the initial state of the nD (**Fig. 15c**), the improvement in the sp² carbon crystallization becomes evident. It is still unclear and would be the subject of a report by itself, to which extent this sp² crystallization would influence the lubricity of this type of particles. However, as can be seen in **Fig. 8** and **Fig. 9**, the COF is not affected by this fact.

Summarizing, the activity of the CNTs during lubrication is noticeable and more marked than the other nanoparticles studied. As already mentioned, this is a result of the different lubrication mechanisms shown by the particles, where only the CNTs could be straightforwardly dragged into the direct tribological contact during relative motion, as opposed to the case of the low aspect ratio particles (OLC and nD).

4 Conclusions

The present study investigates the dominant friction and wear mechanisms in case of dry sliding of carbon nanoparticle (CNT, OLC and nD) reinforced nickel matrix composites under elastic and elasto-plastic contact conditions. For the given materials and geometries and based on calculations using an extended Greenwood-Williamson model (Jackson-Green model), a critical normal load of 0.6 N is found below or above which the contact is either elastic or elasto-plastic. Measurements under elastic conditions were performed under 4% of relative humidity, thus excluding a graphite-based lubrication effect. It is shown that only CNT provide an efficient lubrication as reinforcement phase in composites with the lubrication mechanism being based on sliding and/or rolling of the tube-like particles. No lubrication is observed for “0D” particles, irrespective of their

hybridization, thus the lubrication effect is further traced back to the large aspect ratio of CNT, allowing them to be dragged out of the surface cavities into the local direct tribological contact. For elasto-plastic contact conditions, the formation of dense, cracked, oxide-containing sheets is observed, which do not hinder CNT from efficiently lubricating the system. It is believed, that CNT are able to separate the sheets from each other and from the surface, hence allowing them to slide. The lubrication effect increases with increasing volume content of CNT, reaching a maximum steady state frictional reduction of 50% compared to the unreinforced nickel reference for elastic and elasto-plastic contact conditions for low and medium relative humidities. The present study highlights the potential of CNT as solid lubricant for self-lubricating metal matrix composites.

Acknowledgements

The present work is supported by funding from the Deutsche Forschungsgemeinschaft (DFG, project: MU 959/38-1 and SU 911/1-1). L. R., S.S., and F. M. wish to acknowledge the EFRE Funds of the European Commission for support of activities within the AME-Lab project. Prof. Dr. Volker Presser is acknowledged for providing the possibility to use Raman spectroscopy. This work was supported by the CREATE-*Network Project*, Horizon 2020 of the European Commission (RISE Project No. 644013).

Conflicts of Interest

The authors declare no conflict of interest.

References

- [1] K. Holmberg, P. Andersson, A. Erdemir, Global energy consumption due to friction in passenger cars, *Tribol. Int.* 47 (2012) 221–234. doi:10.1016/j.triboint.2011.11.022.
- [2] C. Donnet, A. Erdemir, Solid Lubricant Coatings: Recent Developments and Future Trends, *Tribol. Lett.* 17 (2004) 389–397. doi: 1023-8883/04/1000–0389/0
- [3] S.M. Aouadi, H. Gao, A. Martine, T.W. Scharf, C. Muratore, Lubricious oxide coatings for extreme temperature applications: A review, *Surf. Coatings Technol.* 257 (2014) 266–277. doi: 10.1016/j.surfcoat.2014.05.064
- [4] J.Y. Hwang, B.K. Lim, J. Tiley, R. Banerjee, S.H. Hong, Interface analysis of ultra-high strength carbon nanotube/nickel composites processed by molecular level mixing, *Carbon* 57 (2013) 282–287. doi:10.1016/j.carbon.2013.01.075.
- [5] S.R. Bakshi, A. Agarwal, An analysis of the factors affecting strengthening in carbon nanotube reinforced aluminum composites, *Carbon* 49 (2011) 533–544. doi:10.1016/j.carbon.2010.09.054.
- [6] D. Nunes, M. Vilarigues, J.B. Correia, P.A. Carvalho, Nickel–carbon nanocomposites: Synthesis, structural changes and strengthening mechanisms, *Acta Mater.* 60 (2012) 737–747. doi:10.1016/j.actamat.2011.10.012.
- [7] D. Nunes, J.B. Correia, P.A. Carvalho, Nanodiamond dispersions in metallic matrices with different carbon affinity, *Microsc. Microanal.* 19 (2013) 2013. doi:10.1017/S1431927613001220.
- [8] V. Livramento, J.B. Correia, N. Shohoji, E. Ōsawa, Nanodiamond as an effective reinforcing component for nano-copper, *Diam. Relat. Mater.* 16 (2007) 202–204. doi:10.1016/j.diamond.2006.05.008.
- [9] J.N. Boland, X.S. Li, Microstructural Characterisation and Wear Behaviour of Diamond Composite

- Materials, *Materials (Basel)*. 3 (2010) 1390–1419. doi:10.3390/ma3021390.
- [10] L. Kumari, T. Zhang, G. Du, W. Li, Q. Wang, A. Datye, K. Wu, Thermal properties of CNT-Alumina nanocomposites, *Compos. Sci. Technol.* 68 (2008) 2178–2183. doi:10.1016/j.compscitech.2008.04.001.
- [11] A. Agarwal, S. Bakshi, D. Lahiri, *Carbon Nanotubes - Reinforced Metal Matrix Composites*, 2011. CRC press, ISBN: 978-1-4398-1149-8
- [12] D. Nunes, J.B. Correia, P.A. Carvalho, Nanodiamond dispersions in nanostructured metals, *Microsc. Microanal.* 18 (2012) 73–74. doi:10.1017/S1431927612013025.
- [13] Y. Li, B.X. Li, W.J. Zou, The Relationship between Nanocrystalline Structure and Frictional Properties of Nanodiamond/Ni Composite Coatings by Brush Plating, *Appl. Mech. Mater.* 80–81 (2011) 683–687. doi:10.4028/www.scientific.net/AMM.80-81.683.
- [14] A. Hirata, N. Yoshioka, Sliding friction properties of carbon nanotube coatings deposited by microwave plasma chemical vapor deposition, *Tribol. Int.* 37 (2004) 893–898. doi:10.1016/j.triboint.2004.07.005.
- [15] K. Miyoshi, K.W.S. Jr., R.L. Vander Wal, R. Andrews, A. Sayir, Solid lubrication by multiwalled carbon nanotubes in air and in vacuum, *Tribol. Lett.* 19 (2005) 191–201. doi:10.1007/s11249-005-6146-4.
- [16] L. Reinert, S. Suárez, A. Rosenkranz, Tribo-Mechanisms of Carbon Nanotubes: Friction and Wear Behavior of CNT-Reinforced Nickel Matrix Composites and CNT-Coated Bulk Nickel, *Lubricants*. 4 (2016) 11. doi:10.3390/lubricants4020011.
- [17] S. Suarez, L. Reinert, F. Mücklich, Carbon Nanotube (CNT)-Reinforced Metal Matrix Bulk Composites: Manufacturing and Evaluation, in: *Diam. Carbon Compos. Nanocomposites*, 2016. doi: 10.5772/63886
- [18] Y. Gogotsi, V. Presser, *Carbon Nanomaterials*, 2014. CRC press, ISBN: 13-978-1-4665-0242-0
- [19] S.R. Bakshi, D. Lahiri, A. Agarwal, Carbon nanotube reinforced metal matrix composites - a review, *Int. Mater. Rev.* 55 (2010) 41–64. doi:10.1179/095066009X12572530170543.
- [20] V.N. Mochalin, O. Shenderova, D. Ho, Y. Gogotsi, The properties and applications of nanodiamonds., *Nat. Nanotechnol.* 7 (2012) 11–23. doi:10.1038/nnano.2011.209.
- [21] S. Iijima, Helical microtubules of graphitic carbon, *Nature*. 354 (1991) 56–58.
- [22] J. Cebik, J.K. McDonough, F. Peerally, R. Medrano, I. Neitzel, Y. Gogotsi, S. Osswald, Raman spectroscopy study of the nanodiamond-to-carbon onion transformation., *Nanotechnology*. 24 (2013) 1–10. doi:10.1088/0957-4484/24/20/205703.
- [23] M. Zeiger, N. Jäckel, M. Aslan, D. Weingarh, V. Presser, Understanding structure and porosity of nanodiamond-derived carbon onions, *Carbon* 84 (2015) 584–598. doi:10.1016/j.carbon.2014.12.050.
- [24] K.T. Kim, S. Il Cha, S.H. Hong, Hardness and wear resistance of carbon nanotube reinforced Cu matrix nanocomposites, *Mater. Sci. Eng. A*. 449–451 (2007) 46–50. doi:10.1016/j.msea.2006.02.310.
- [25] X.H. Chen, J. Peng, F. Deng, J. Wang, W. Li, Tribological behavior of carbon nanotubes — reinforced nickel matrix composite coatings, *J. Mater. Sci. Lett.* 20 (2001) 2057–2060.
- [26] X.H. Chen, C.S. Chen, H.N. Xiao, H.B. Liu, L.P. Zhou, S.L. Li, G. Zhang, Dry friction and wear characteristics of nickel/carbon nanotube electroless composite deposits, *Tribol. Int.* 39 (2006) 22–28. doi:10.1016/j.triboint.2004.11.008.
- [27] S. Arai, A. Fujimori, M. Murai, M. Endo, Excellent solid lubrication of electrodeposited nickel-multiwalled carbon nanotube composite films, *Mater. Lett.* 62 (2008) 3545–3548. doi:10.1016/j.matlet.2008.03.047.

- [28] A. Sanaty-Zadeh, Comparison between current models for the strength of particulate-reinforced metal matrix nanocomposites with emphasis on consideration of Hall–Petch effect, *Mater. Sci. Eng. A*. 531 (2012) 112–118. doi:10.1016/j.msea.2011.10.043.
- [29] M.R. Falvo, R.M.T. Li, A. Helser, V. Chi, Nanometre-scale rolling and sliding of carbon nanotubes, *Nature*. 397 (1999) 1–3.
- [30] T.W. Scharf, A. Neira, J.Y. Hwang, J. Tiley, R. Banerjee, Self-lubricating carbon nanotube reinforced nickel matrix composites, *J. Appl. Phys.* 106 (2009) 13508. doi:10.1063/1.3158360.
- [31] J.J. Hu, S.H. Jo, Z.F. Ren, A. Voevodin, J.S. Zabinski, Tribological behavior and graphitization of carbon nanotubes grown on 440C stainless steel, *Tribol. Lett.* 19 (2005) 119–125. doi:10.1007/s11249-005-5091-6.
- [32] F. Colonna, A. Fasolino, E.J. Meijer, Graphitization of single-wall nanotube bundles at extreme conditions: Collapse or coalescence route, *Phys. Rev. B*. 88 (2013) 165416. doi:10.1103/PhysRevB.88.165416.
- [33] P.L. Dickrell, S.K. Pal, G.R. Bourne, C. Muratore, a. a. Voevodin, P.M. Ajayan, L.S. Schadler, W.G. Sawyer, Tunable friction behavior of oriented carbon nanotube films, *Tribol. Lett.* 24 (2006) 85–90. doi:10.1007/s11249-006-9162-0.
- [34] C.-C. Chou, S.-H. Lee, Tribological behavior of nanodiamond-dispersed lubricants on carbon steels and aluminum alloy, *Wear*. 269 (2010) 757–762. doi:10.1016/j.wear.2010.08.001.
- [35] L. Wang, Y. Gao, Q. Xue, H. Liu, T. Xu, Effects of nano-diamond particles on the structure and tribological property of Ni-matrix nanocomposite coatings, *Mater. Sci. Eng. A*. 390 (2005) 313–318. doi:10.1016/j.msea.2004.08.033.
- [36] V.Y. Dolmatov, T. Fujimura, G.K. Burkat, E.A. Orlova, M. V Veretennikova, Preparation of wear-resistant chromium coatings using different types of Nanodiamonds, *Powder Metall. Met. Ceram.* 42 (2003) 55–59. doi: 1068-1302/03/1112-0587
- [37] S. Park, D. Srivastava, K. Cho, Generalized Chemical Reactivity of Curved Surfaces: Carbon Nanotubes, *Nano Lett.* 3 (2003) 1273–1277. doi:10.1021/nl0342747.
- [38] K.W. Street, M. Marchetti, R.L. Vander Wal, A.J. Tomasek, Evaluation of the tribological behavior of nano-onions in Krytox 143AB, *Tribol. Lett.* 16 (2004) 143–149. doi: 1023-8883/04/0200–0143/0
- [39] A. Hirata, M. Igarashi, T. Kaito, Study on solid lubricant properties of carbon onions produced by heat treatment of diamond clusters or particles, *Tribol. Int.* 37 (2004) 899–905. doi:10.1016/j.triboint.2004.07.006.
- [40] E.W. Bucholz, S.R. Phillpot, S.B. Sinnott, Molecular dynamics investigation of the lubrication mechanism of carbon nano-onions, *Comput. Mater. Sci.* 54 (2012) 91–96. doi:10.1016/j.commatsci.2011.09.036.
- [41] L. Reinert, M. Zeiger, S. Suarez, V. Presser, F. Mücklich, Dispersion analysis of carbon nanotubes, carbon onions, and nanodiamonds for their application as reinforcement phase in nickel metal matrix composites, *RSC Adv.* 5 (2015) 95149–95159. doi:10.1039/C5RA14310A.
- [42] L. Reinert, S. Suarez, T. Müller, F. Mücklich, Carbon Nanoparticle-Reinforced Metal Matrix Composites: Microstructural Tailoring and Predictive Modeling, *Adv. Eng. Mater.* 19 (2017) 1–6. doi:10.1002/adem.201600750.
- [43] S. Suarez, F. Lasserre, F. Mücklich, Mechanical properties of MWNT/Ni bulk composites: Influence of

- the microstructural refinement on the hardness, *Mater. Sci. Eng. A.* 587 (2013) 381–386. doi:10.1016/j.msea.2013.08.058.
- [44] J. Greenwood, J. Williamson, Contact of nominally flat surfaces, *Proc. R. Soc. London.* 295 (1966) 300–319. doi:10.1098/rspa.1966.0242.
- [45] L. Kogut, I. Etsion, Elastic-Plastic Contact Analysis of a Sphere and a Rigid Flat, *J. Appl. Mech.* 69 (2002) 657–662.
- [46] W.R. Chang, I. Etsion, D.B. Bogy, An Elastic-Plastic Model for the Contact of Rough Surfaces, *J. Tribol.* 109 (1987) 257–263.
- [47] Y. Zhao, D.M. Maietta, L. Chang, An Asperity Microcontact Model Incorporating the Transition From Elastic Deformation to Fully Plastic Flow, *J. Tribol.* 122 (1999) 86–93.
- [48] R.L. Jackson, I. Green, A statistical model of elasto-plastic asperity contact between rough surfaces, *Tribol. Int.* 39 (2006) 906–914. doi:10.1016/j.triboint.2005.09.001.
- [49] J.I. McCool, Relating Profile Instrument Measurements to the Functional Performance of Rough Surfaces, *Trans. ASME.* 109 (1987) 264–270.
- [50] R. Jackson, I. Green, On the modeling of elastic contact between rough surfaces, *Tribol. Trans.* 54 (2011) 300–314. doi:10.1080/10402004.2010.542277.
- [51] I. Green, Poisson ratio effects and critical valus in spherical and cylindrical Hertzian contacts, *Int. J. Appl. Mech. Eng.* 10 (2005) 451–462.
- [52] H. Hertz, Über die Berührung von elastischen festen Körpern, *J. Für Die Reine Und Angew. Math.* 92. (1881).
- [53] R. Jackson, M. ASME, I. Chusoipin, I. Green, A Finite Element Study of the Residual Sress and Deformation in Hemispherical Contacts, *J. Tribol.* 127 (2005). doi:10.1115/1.1843166.
- [54] D. Berman, A. Erdemir, A. V. Sumant, Graphene: A new emerging lubricant, *Mater. Today.* 17 (2014) 31–42. doi:10.1016/j.mattod.2013.12.003.
- [55] B.K. Yen, T. Ishihara, Effect of humidity on friction and wear of Al-Si eutectic alloy and Al-Si alloy-graphite composites, *Wear.* 198 (1996) 169–175.
- [56] R.H. Savage, Graphite Lubrication, *J. Appl. Phys.* 19 (1948) 1. doi:10.1063/1.1697867.
- [57] S.R. Sails, D.J. Gardiner, M. Bowden, J. Savage, D. Rodway, Monitoring the quality of diamond films using Raman spectra excited at 514.5 nm and 633 nm, *Diam. Relat. Mater.* 5 (1996) 589–591. doi:10.1016/0925-9635(96)90031-X.
- [58] O.O. Mykhaylyk, Y.M. Solonin, D.N. Batchelder, R. Brydson, Transformation of nanodiamond into carbon onions: A comparative study by high-resolution transmission electron microscopy, electron energy-loss spectroscopy, x-ray diffraction, small-angle x-ray scattering, and ultraviolet Raman spectroscopy, *J. Appl. Phys.* 97 (2005) 1–16. doi:10.1063/1.1868054.
- [59] A. Ferrari, J. Robertson, Resonant Raman spectroscopy of disordered, amorphous, and diamondlike carbon, *Phys. Rev. B.* 64 (2001) 75414. doi:10.1103/PhysRevB.64.075414.
- [60] K. Johnson, *Contact mechanics*, Cambridge Univ. Press, 1985. ISBN: 0-521-25576-7
- [61] R.L. Jackson, I. Green, A Finite Element Study of Elasto-Plastic Hemispherical Contact Against a Rigid Flat, *J. Tribol.* 127 (2005) 343–354.
- [62] F. Banhart, Interactions between metals and carbon nanotubes: at the interface between old and new materials., *Nanoscale.* 1 (2009) 201–13. doi:10.1039/b9nr00127a.

- [63] P.J. Blau, On the nature of running-in, *Tribol. Int.* 38 (2005) 1007–1012. doi:10.1016/j.triboint.2005.07.020.
- [64] M. Shafiei, A.T. Alpas, Friction and Wear Mechanisms of Nanocrystalline Nickel in Ambient and Inert Atmospheres, *Metall. Mater. Trans. A.* 38 (2007) 1621–1631. doi:10.1007/s11661-007-9157-y.
- [65] L. Reinert, S. Schütz, S. Suarez, F. Mücklich, Influence of Surface Roughness on the Lubrication Effect of Carbon Nanoparticle-Coated Steel Surfaces, *Tribol. Lett.* 66 (2018). doi:10.1007/s11249-018-1001-6.
- [66] A. Ferrari, J. Robertson, Interpretation of Raman spectra of disordered and amorphous carbon, *Phys. Rev. B.* 61 (2000) 14095–14107. doi:10.1103/PhysRevB.61.14095.
- [67] S. Suarez, L. Reinert, M. Zeiger, V. Presser, P. Miska, F. Müller, F. Mücklich, In-situ nanodiamond to onion-like carbon transformation in metal matrix composites, *Carbon* 129 (2017) 631-636. doi 10.1016/j.carbon.2017.12.072